

Current-induced dynamics of composite free layer with antiferromagnetic interlayer exchange coupling

P. Baláž¹ and J. Barnaś^{1,2}

¹*Department of Physics, Adam Mickiewicz University, Umultowska 85, 61-614 Poznań, Poland*

²*Institute of Molecular Physics, Polish Academy of Sciences Smoluchowskiego 17, 60-179 Poznań, Poland*

(Dated: January 11, 2013)

Current-induced dynamics in spin valves including composite free layer with antiferromagnetic interlayer exchange coupling is studied theoretically within the diffusive transport regime. We show that current-induced dynamics of a synthetic antiferromagnet is significantly different from dynamics of a synthetic ferrimagnet. From macrospin simulations we obtain conditions for switching the composite free layer, as well as for appearance of various self-sustained dynamical modes. Numerical simulations are compared with simple analytical models of critical current based on linearized Landau-Lifshitz-Gilbert equation.

PACS numbers: 67.30.hj, 75.60.Jk, 75.70.Cn

I. INTRODUCTION

After the effect of spin transfer torque (STT) in thin magnetic films had been predicted^{1,2} and then experimentally proven^{3,4}, it was generally believed that current-controlled spin valve devices would replace soon the memory cells operated by external magnetic field. Such a technological progress, if realized, would certainly offer higher data storage density and faster manipulation with the information stored on a hard drive memory. However, it became clear soon that some important issues must be solved before devices based on spin torque could be used in practice. The most important is the reduction of current density needed for magnetic excitation (switching) in thin films, as well as enhancement of switching efficiency and thermal stability. Some progress has been made by using more complex spin valve structures and/or various subtle switching schemes based on optimized current and field pulses⁵⁻⁸.

A significant enhancement of thermal stability can be achieved by replacing a simple free layer (single homogeneous layer) with a system of two magnetic films separated by a thin nonmagnetic spacer, known as composite free layer (CFL). The spacer layer is usually thin so there is a strong RKKY exchange coupling between magnetic layers^{9,10}. In practice, antiferromagnetic configuration is preferred as it reduces the overall magnetic moment of the CFL structure and makes the system less vulnerable to external magnetic fields and thermal agitation. When the antiferromagnetically coupled magnetic layers are identical, we call the structure synthetic antiferromagnet (SyAF). If they are different, then the CFL has uncompensated magnetic moment and such a system will be referred to as synthetic ferrimagnet (SyF).

Current and/or field induced dynamics of CFLs is currently a subject of both experimental and theoretical investigations¹¹⁻¹⁴. Switching scheme of SyAF by magnetic field pulses has been proposed in Ref. [11], and then the possibility of current-induced switching of SyAF was demonstrated experimentally¹². In turn, the possi-

bility of critical current reduction has been shown for a CFL with ferromagnetically coupled magnetic layers¹⁵. However, the reduction of critical current in the case of antiferromagnetically coupled CFLs still remains an open problem. In a recent numerical study on switching a SyAF free layer¹⁶ it has been shown that the corresponding critical current in most cases is higher than the current required for switching of a simple free layer, and only in a narrow range of relevant parameters (exchange coupling, layer thickness, etc.) the critical current is reduced. Hence, proper understanding of current-induced dynamics of CFLs is highly required. We also note, that CFL can be used as a polarizer, too. Indeed, it has been shown recently¹⁷ that SyAF used as a reference layer (with magnetic moment fixed fixed to adjacent antiferromagnetic layer due to exchange anisotropy) might be excited due to dynamical coupling¹⁸ with a simple sensing layer^{19,20}.

The main objective of this paper is to study current-induced dynamics of a CFL with antiferromagnetic RKKY coupling in metallic spin valve pillars. We consider a system AF/F₀/N₁/F₁/N₂/F₂, shown in Fig. 1, where AF is an antiferromagnetic layer (used to bias magnetization of the reference magnetic layer F₀), F₁ and F₂ are two magnetic layers, while N₁ and N₂ are non-magnetic spacers. The part F₁/N₂/F₂ constitutes the CFL structure with antiferromagnetic interlayer exchange coupling. We examine current-induced dynamics of both SyAF and SyF free layers. These two structures differ only in the thickness of F₁ layer, while RKKY coupling and other pillar parameters remain the same.

We assume that spin-dependent electron transport is diffusive in nature, and employ the model described in Refs. [21] and [22]. An important advantage of this model is the fact that it enables calculating spin current components and spin accumulation consistently in all magnetic and nonmagnetic layers, as well as current-induced torques exerted on all magnetic components. The torques acting at the internal interfaces of CFL introduce additional dynamical coupling between the corresponding

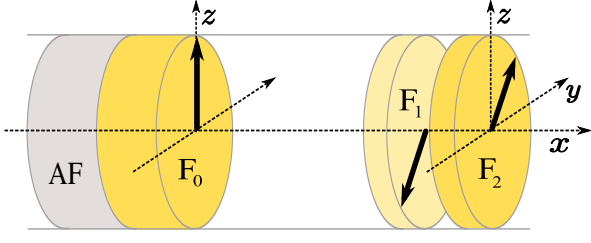


FIG. 1. Scheme of the spin valve pillar structure with a composite free layer.

magnetic layers. Consequently, the magnetic dynamics of CFL has been modelled by two coupled macrospins and described in terms of Landau-Lifshitz-Gilbert (LLG) equation. In addition, we derive some analytical expressions for critical currents from the stability conditions of linearized LLG equation in the static points^{23,24}, and discuss results in the context of numerical simulations.

The paper is organized as follows. In section 2 we describe the assumed models for spin dynamics and STT calculations. In section 3 we analyze STT acting on CFL and present results from numerical simulations on current-induced switching and magnetic dynamics. Some additional information on STT calculation can be found in the Appendix. Critical currents are derived and discussed in section 4. Finally, summary and general conclusions are in section 5.

II. MAGNETIZATION DYNAMICS

In the macrospin approximation, magnetization dynamics of the CFL is described by two coupled Landau-Lifshitz-Gilbert (LLG) equations,

$$\begin{aligned} \frac{d\hat{\mathbf{S}}_i}{dt} + \alpha\hat{\mathbf{S}}_i \times \frac{d\hat{\mathbf{S}}_i}{dt} &= \mathbf{\Gamma}_i, \\ \mathbf{\Gamma}_i &= -|\gamma_g|\mu_0\hat{\mathbf{S}}_i \times \mathbf{H}_{\text{eff}i} + \frac{|\gamma_g|}{M_s d_i} \boldsymbol{\tau}_i, \end{aligned} \quad (1)$$

for $i = 1, 2$, where $\hat{\mathbf{S}}_i$ stands for a unit vector along the net spin moment of the i -th layer, whereas $\mathbf{H}_{\text{eff}i}$ and $\boldsymbol{\tau}_i$ are the effective field and current-induced torque, respectively, both acting on $\hat{\mathbf{S}}_i$. The damping parameter α and the saturation magnetization M_s are assumed the same for both magnetic components of the CFL. Furthermore, γ_g is the gyromagnetic ratio, μ_0 is the vacuum permeability, and d_i stands for thickness of the F_i layer.

The effective magnetic field for the F_i layer is

$$\begin{aligned} \mathbf{H}_{\text{eff}i} &= -H_{\text{app}}\hat{\mathbf{e}}_z - H_{\text{ani}}(\hat{\mathbf{S}}_i \cdot \hat{\mathbf{e}}_z)\hat{\mathbf{e}}_z + \mathbf{H}_{\text{dem}i}(\hat{\mathbf{S}}_i) \\ &+ \mathbf{H}_{\text{int}i}(\hat{\mathbf{S}}_0, \hat{\mathbf{S}}_j) + H_{\text{RKKY}i}\hat{\mathbf{S}}_j, \end{aligned} \quad (2)$$

where $i, j = 1, 2$ and $i \neq j$. In the latter equation, H_{app} is the external magnetic field applied along the easy axis in the layers' plane (and oriented opposite to the axis z), H_{ani} is the uniaxial anisotropy field (the same for

both magnetic layers), and $\mathbf{H}_{\text{dem}i} = (\bar{\mathbf{N}}_i \cdot \hat{\mathbf{S}}_i)M_s$ is the self-demagnetization field of the F_i layer with $\bar{\mathbf{N}}_i$ being the corresponding demagnetization tensor. Similarly, $\mathbf{H}_{\text{int}i} = (\bar{\mathbf{N}}_{0i} \cdot \hat{\mathbf{S}}_0)M_{s0} + (\bar{\mathbf{N}}_{ji} \cdot \hat{\mathbf{S}}_j)M_s$ describes the magnetostatic influence of the layers F_0 and F_j on the layer F_i , respectively. Here, M_{s0} is the saturation magnetization of the layer F_0 , which might be generally different from M_s . Components of the tensors $\bar{\mathbf{N}}_i$, $\bar{\mathbf{N}}_{0i}$ and $\bar{\mathbf{N}}_{ij}$ used in our simulations have been determined by the numerical method introduced by Newell *et al.*²⁵. This method was originally developed for magnetic systems with non-uniform magnetization. To implement it into a macrospin model we considered discretized magnetic layers with uniform magnetizations, calculated tensors in each cell of the layer, and then averaged them along the whole layer. Since these tensors are diagonal, the demagnetization and magnetostatic fields can be expressed as $\mathbf{H}_{\text{dem}i} = (H_{ix}^d S_{ix}, H_{iy}^d S_{iy}, H_{iz}^d S_{iz})$, and $\mathbf{H}_{\text{int}i} = (H_x^{0i} S_{0x}, H_y^{0i} S_{0y}, H_z^{0i} S_{0z}) + (H_x^{ji} S_{jx}, H_y^{ji} S_{jy}, H_z^{ji} S_{jz})$, with S_{ix} , S_{iy} , and S_{iz} denoting the components of the vector $\hat{\mathbf{S}}_i$ ($i = 0, 1, 2$) in the coordinate system shown in Fig.1. Finally, $H_{\text{RKKY}i}$ stands for the RKKY exchange field acting on $\hat{\mathbf{S}}_i$, which is related to the RKKY coupling constant as $H_{\text{RKKY}i} = -J_{\text{RKKY}}/(\mu_0 M_s d_i)$ ¹⁹.

To include thermal effects we add to the effective field (2) a stochastic thermal field $\mathbf{H}_{\text{th}i} = (H_{\text{th}ix}, H_{\text{th}iy}, H_{\text{th}iz})$. For both spins its components obey the rules for Gaussian random processes $\langle H_{\text{th}i\zeta}(t) \rangle = 0$ and $\langle H_{\text{th}i\zeta}(t) H_{\text{th}j\xi}(t') \rangle = 2D\delta_{ij}\delta_{\zeta\xi}\delta(t - t')$, where $i, j = 1, 2$ and $\zeta, \xi = x, y, z$. Here, D is the noise amplitude, which is related to the effective temperature, T_{eff} , as

$$D = \frac{\alpha k_B T_{\text{eff}}}{\gamma_g \mu_0^2 M_s V_i}, \quad (3)$$

where k_B is the Boltzmann constant, and V_i is the volume of F_i layer.

In general, the current-induced torques acting on $\hat{\mathbf{S}}_1$ and $\hat{\mathbf{S}}_2$ can be expressed as a sum of their in-plane and out-of-plane components $\boldsymbol{\tau}_1 = \boldsymbol{\tau}_{1\parallel} + \boldsymbol{\tau}_{1\perp}$ and $\boldsymbol{\tau}_2 = \boldsymbol{\tau}_{2\parallel} + \boldsymbol{\tau}_{2\perp}$, respectively. In a CFL structure, the layer F_1 is influenced by STT induced by the polarizer F_0 , as well as by STT due to the layer F_2 . In turn, the layer F_2 is influenced by the torques from the layer F_1 . Hence we can write

$$\boldsymbol{\tau}_{1\parallel} = I\hat{\mathbf{S}}_1 \times \left[\hat{\mathbf{S}}_1 \times \left(a_1^{(0)}\hat{\mathbf{S}}_0 + a_1^{(2)}\hat{\mathbf{S}}_2 \right) \right], \quad (4a)$$

$$\boldsymbol{\tau}_{1\perp} = I\hat{\mathbf{S}}_1 \times \left(b_1^{(0)}\hat{\mathbf{S}}_0 + b_1^{(2)}\hat{\mathbf{S}}_2 \right), \quad (4b)$$

$$\boldsymbol{\tau}_{2\parallel} = Ia_2^{(1)}\hat{\mathbf{S}}_2 \times \left(\hat{\mathbf{S}}_2 \times \hat{\mathbf{S}}_1 \right), \quad (4c)$$

$$\boldsymbol{\tau}_{2\perp} = Ib_2^{(1)}\hat{\mathbf{S}}_2 \times \hat{\mathbf{S}}_1, \quad (4d)$$

where I is the charge current density, which is positive when electrons flow from the layer F_2 towards F_0 (see Fig. 1), while the parameters $a_i^{(j)}$ and $b_i^{(j)}$ ($i, j = 1, 2$) are independent of current I , but generally depend on magnetic configuration.

We write the current density in the spin space as $\mathbf{j} = j_0 \mathbf{1} + \mathbf{j} \cdot \boldsymbol{\sigma}$, where j_0 is the particle current density ($I = ej_0$), \mathbf{j} is the spin current density (in the units of $\hbar/2$), $\boldsymbol{\sigma}$ is the vector of Pauli matrices, and $\mathbf{1}$ is a 2×2 unit matrix. In frame of the diffusive transport model²¹, the parameters $a_i^{(j)}$ and $b_i^{(j)}$ are given by the formulas

$$\begin{aligned} a_1^{(0)} &= -\frac{\hbar}{2} \frac{j'_{1y} |_{N_1/F_1}}{I \sin \theta_{01}}, & b_1^{(0)} &= \frac{\hbar}{2} \frac{j'_{1x} |_{N_1/F_1}}{I \sin \theta_{01}}, \\ a_1^{(2)} &= -\frac{\hbar}{2} \frac{j''_{2y} |_{F_1/N_2}}{I \sin \theta_{12}}, & b_1^{(2)} &= \frac{\hbar}{2} \frac{j''_{2x} |_{F_1/N_2}}{I \sin \theta_{12}}, \\ a_2^{(1)} &= -\frac{\hbar}{2} \frac{j'''_{2y} |_{N_2/F_2}}{I \sin \theta_{12}}, & b_2^{(1)} &= \frac{\hbar}{2} \frac{j'''_{2x} |_{N_2/F_2}}{I \sin \theta_{12}}, \end{aligned} \quad (5)$$

where the angles θ_{01} and θ_{12} are given by $\cos \theta_{01} = \hat{\mathbf{S}}_0 \cdot \hat{\mathbf{S}}_1$ and $\cos \theta_{12} = \hat{\mathbf{S}}_1 \cdot \hat{\mathbf{S}}_2$. Here, j'_{1y} and j'_{1x} are transversal (to $\hat{\mathbf{S}}_1$) components of spin current in the layer N_1 (taken at the N_1/F_1 interface) written in the local coordinate system of $\hat{\mathbf{S}}_1$. Thus, j'_{1y} is parallel to the vector $\hat{\mathbf{S}}_1 \times (\hat{\mathbf{S}}_1 \times \hat{\mathbf{S}}_0)$ (lying in the plane defined by $\hat{\mathbf{S}}_0$ and $\hat{\mathbf{S}}_1$) and j'_{1x} is aligned with $\hat{\mathbf{S}}_1 \times \hat{\mathbf{S}}_0$ (perpendicular to the plane defined by $\hat{\mathbf{S}}_0$ and $\hat{\mathbf{S}}_1$). Note, that the z -component of spin current is aligned along $\hat{\mathbf{S}}_1$ and does not contribute to STT²⁶. Similarly, we define the torque amplitudes acting inside the CFL. Here, j''_{2y} and j''_{2x} are the components of spin current in the layer N_2 (taken at the N_2/F_1 interface), transversal to $\hat{\mathbf{S}}_1$ and lying respectively in the plane and perpendicularly to the plane defined by $\hat{\mathbf{S}}_1$ and $\hat{\mathbf{S}}_2$. Analogically, j'''_{2y} and j'''_{2x} are spin current components in N_2 transversal to $\hat{\mathbf{S}}_2$. The relevant spin current transformations are given in Appendix A. Note, that the spin current components depend linearly on I , so the parameters $a_i^{(j)}$ and $b_i^{(j)}$ are independent of the current density I .

III. NUMERICAL SIMULATIONS

In this section we present results on our numerical simulations of current-induced dynamics for two metallic pillar structures including CFL with antiferromagnetic interlayer exchange coupling. As described in the introduction, the considered pillars have the general structure AF/ $F_0/N_1/F_1/N_2/F_2$ (see Fig.(1)). More specifically, we consider spin valves Cu - IrMn(10)/Py(8)/Cu(8)/Co(d_1)/Ru(1)/Co(d_2) - Cu, where the numbers in brackets stand for the layer thicknesses in nanometers. The layer Py(8) is the Permalloy polarizing layer with its magnetization fixed due to exchange coupling to IrMn. In turn, Co(d_1)/Ru(1)/Co(d_2) is the CFL ($F_1/N_2/F_2$ structure) with antiferromagnetic RKKY exchange coupling *via* the thin ruthenium layer. The coupling constant between Co layers has been assumed as $J_{\text{RKKY}} \simeq -0.6 \text{ mJ/m}^2$, which is close to experimentally observed values^{19,20}. Here, we shall analyze two different geometries of CFL. The first one is a SyAF

structure with $d_1 = d_2 = 2 \text{ nm}$, while the second one is a synthetic ferrimagnet (SyF) with $d_1 = 2d_2 = 4 \text{ nm}$.

Simulations have been based on numerical integration of the two coupled LLG equations (1) with simultaneous calculations of STT, see Eq.(4). We have assumed typical values of the relevant parameters, i.e., the damping parameter has been set to $\alpha = 0.01$, while the uniaxial anisotropy field $H_{\text{ani}} = 45 \text{ kAm}^{-1}$ in both magnetic layers of the CFL. In turn, saturation magnetization of cobalt has been assumed as $M_s(\text{Co}) = 1.42 \times 10^6 \text{ Am}^{-1}$, and for permalloy $M_s(\text{Py}) = 6.92 \times 10^5 \text{ Am}^{-1}$. The demagnetization field and magnetostatic interaction of magnetic layers have been calculated for layers of elliptical cross-section, with the major and minor axes equal to 130 nm and 60 nm, respectively.

For both structures under consideration we have analyzed the current-induced dynamics as a function of current density and external magnetic field. The results have been presented in the form of diagrams displaying time-averaged values of the pillar resistance. Numerical integration of Eq.(1) has been performed using corrector-predictor Heun scheme, and the results have been verified for integration steps in the range from 10^{-4} ns up to 10^{-6} ns . The STT components acting on CFL spins have been calculated at each integration step from the spin currents, which have been numerically calculated from the appropriate boundary conditions²¹. Similarly, resistance of the studied pillars has been calculated from spin accumulation in frame of the model used also for the STT description (for details see also Ref. 27).

A. Spin transfer torque

Let us analyze first the angular dependence of STT components in the structures under consideration. Although the thicknesses of magnetic layers in the studied SyAF and SyF structures are different, the angular dependence of STT components as well as their amplitudes are very similar. Thus, the analysis of STT in SyAF applies also qualitatively to the studied SyF free layer.

First, we analyze STT components in the case when SyAF is rotated as a rigid structure, i.e. the antiparallel configuration of $\hat{\mathbf{S}}_1$ and $\hat{\mathbf{S}}_2$ is maintained. To have a nonzero torque between F_1 and F_2 layers, $\hat{\mathbf{S}}_2$ has been tilted away from the antiparallel configuration by an angle of 1° . Figure 2 shows all three cartesian components (see Fig.1 for definition of the coordinate system) of STT acting at N/F interfaces as a function of the angle θ between $\hat{\mathbf{e}}_z$ and $\hat{\mathbf{S}}_1$. While the y and z -components are in the plane of the layers (the spins of CFL are rotated in the layer plane), the component x is normal to the layer plane. However, τ_x remains negligible at all interfaces of the CFL. The STT acting at N_1/F_1 reveals a standard (non-wavy²⁸) angular dependence, and vanishes when $\hat{\mathbf{S}}_1$ is collinear with $\hat{\mathbf{S}}_0$. Its amplitude is comparable to STT in standard spin valves with a simple free layer. The STT at F_1/N_2 and N_2/F_2 interfaces also depends on the an-

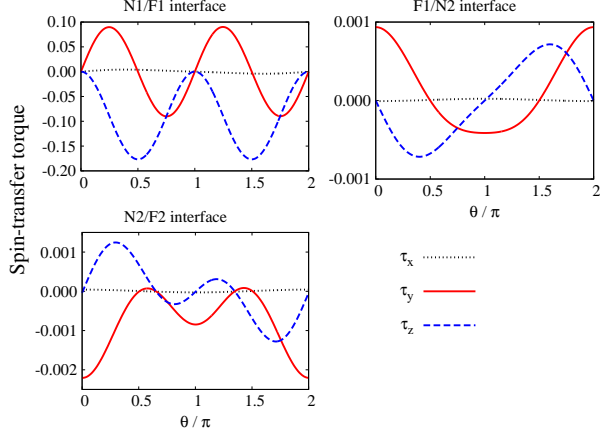


FIG. 2. (color online) Angular dependence of the cartesian components of STT, in the units of $\hbar I/|e|$, acting at N/F interfaces, when magnetization of the SyAF structure is rotated rigidly with both \hat{S}_1 and \hat{S}_2 remaining in the corresponding layer planes. Here, θ is an angle between \hat{S}_1 and \hat{e}_z . \hat{S}_2 is tilted away from the antiparallel configuration with \hat{S}_1 by an angle of 1° .

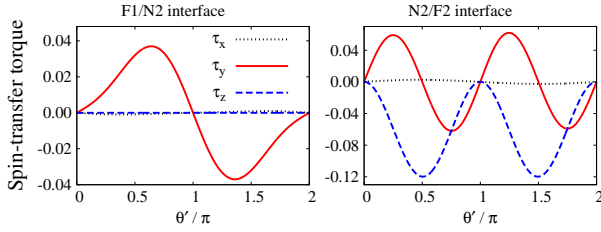


FIG. 3. (color online) Angular dependence of the cartesian STT components in the units of $\hbar I/|e|$ acting on F1/N2 and N2/F1 interfaces when $\hat{S}_0 = \hat{S}_1 = \hat{e}_z$ and \hat{S}_2 is rotated from \hat{e}_z in the layer's plane by an angle θ' .

gle θ . However, they are about two order of magnitude smaller, which is a consequence of a small angle (1°) assumed between \hat{S}_1 and \hat{S}_2 .

As will be shown in the following, CFL is usually not switched as a rigid structure, but generally forms a configuration which deviates from the antiparallel one. Figure 3 shows how the STT components at the F1/N2 and N2/F2 interfaces vary when \hat{S}_2 is rotated from \hat{e}_z by an angle θ' , while \hat{S}_1 remains fixed and is parallel to $\hat{S}_0 = \hat{e}_z$. In such a case, the torque acting at N1/F1 interface remains zero, as \hat{S}_1 stays collinear to \hat{S}_0 . As before, the out-of-plane components are also negligible in comparison to the in-plane ones. The in-plane components of STT reveal standard angular dependence at both interfaces. The amplitude of STT at the internal interfaces of CFL is comparable to that acting at the N1/F1 interface in the case of noncollinear configuration of \hat{S}_0 and \hat{S}_1 , when \hat{S}_2 is fixed in the direction antiparallel to \hat{S}_0 .

When \hat{S}_1 is noncollinear to \hat{S}_0 , the spin accumulation

in N_1 layer increases and consequently the amplitude of STT at F1/N2 and N2/F2 decreases. In turn, when \hat{S}_1 is antiparallel to \hat{S}_0 , the STT inside the CFL structure is reduced by more than a factor of 2. Nonetheless, the STT acting at the internal interfaces of the studied CFL layers might have a significant effect on their current-induced dynamics and switching process, provided the magnetic configuration of CFL might deviate remarkably from its initial antiparallel configuration.

B. Synthetic antiferromagnet

First, we examine dynamics of the SyAF free layer. From symmetry we have $H_{\text{RKKY}1} = H_{\text{RKKY}2} \equiv H_{\text{RKKY}}$, and we have set $H_{\text{RKKY}} = 2 \text{ kOe}$, which corresponds to $J_{\text{RKKY}} \sim -0.6 \text{ mJ/m}^2$. We have performed a number of independent numerical simulations modelling SyAF dynamics induced by constant current and constant in-plane external magnetic field. The latter is assumed to be smaller than the critical field for transition to spin-flop phase of SyAF. Accordingly, each simulation started from an initial state close to $\hat{S}_1 = -\hat{S}_2 = -\hat{e}_z$. To have a non-zero initial STT for \hat{S}_1 , both spins of the SyAF have been tilted by 1° in the layer plane so that they remained collinear.

From the results of numerical simulations we have constructed a map of time-averaged resistance, shown in Fig. 4(a). The resistance has been averaged in the time interval of 30 ns following initial 50 ns equilibration time of the dynamics. The diagram shows only that part of the resistance, which depends on magnetic configuration, and hence varies with CFL dynamics²⁷. The constant part of resistance, due to bulk and interfacial resistances of the studied structure, has been calculated to be as large as $R_{\text{sp}} = 19.74 \text{ k}\Omega\text{m}^2$. For the assumed initial configuration, magnetic dynamics has been observed only for negative current density. When the current is small, no dynamics is observed since the spin motion is damped into the closest collinear state ($\hat{S}_1 = -\hat{S}_2 = -\hat{e}_z$, marked as $\downarrow\uparrow$) of high resistance. After exceeding a certain threshold value of current density, there is a drop in the averaged resistance, which indicates current induced dynamics of the SyAF free layer. Figures 4(b) and (f) show that this drop is associated with switching of the whole SyAF structure into an opposite state ($\hat{S}_1 = -\hat{S}_2 = \hat{e}_z$, marked as $\uparrow\downarrow$).

From Fig. 4(a) follows that the threshold current for dynamics onset markedly depends on the applied field and reaches maximum at a certain value of H_{app} , $H_{\text{app}} = H_0$. Furthermore, it appears that mechanisms of the switching process for $H_{\text{app}} < H_0$ and $H_{\text{app}} > H_0$ are qualitatively different. To distinguish these two mechanisms, we present in Figs. 4(b – i) basic characteristics of switching, calculated for $I = -1.0 \times 10^8 \text{ Acm}^{-2}$ and for fields $H_{\text{app}} = -400 \text{ Oe}$, which is below H_0 [Figs. 4(b – e)], and $H_{\text{app}} = 400 \text{ Oe}$, which lies above H_0 [Figs. 4(f – i)]. Figs. 4(b) and (f) present time evolution of the z-components of both spins. To better understand

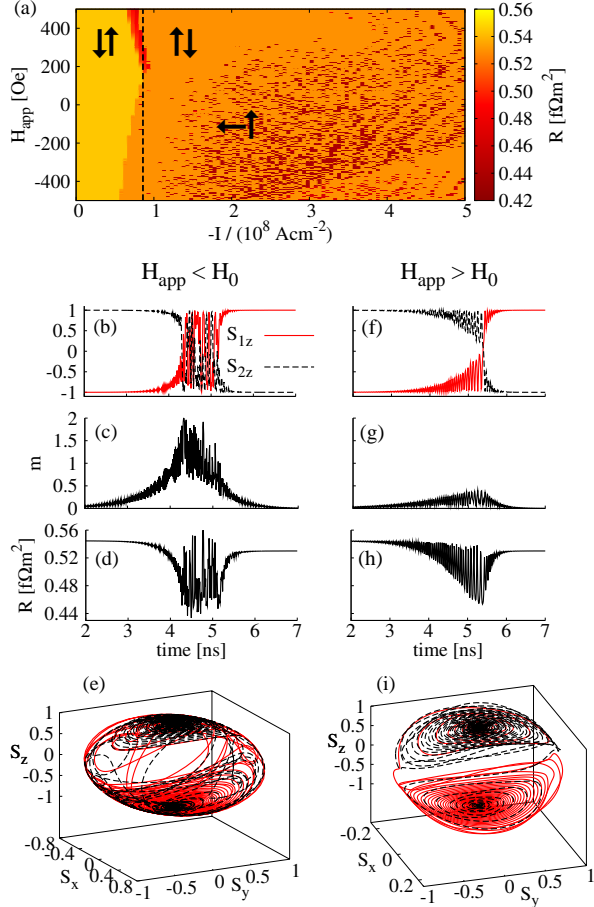


FIG. 4. (color online) (a) Averaged resistance of Cu-IrMn(10)/Py(8)/Cu(8)/Co(2)/Cu(1)/Co(2)-Cu spin valve pillar with a SAF free layer as a function of current density and applied magnetic field. Examples of switching processes at $I = -1.0 \times 10^8 \text{ Acm}^{-2}$ and $H_{\text{app}} = -400 \text{ Oe}$ (b – e) and $H_{\text{app}} = 400 \text{ Oe}$ (f – i). Figures (b) and (f) show dynamics of z -components of both spin moments, (c) and (g) present the overall magnetization of the free layer, (d) and (h) show the corresponding variation of pillar resistance, (e) and (i) show the spin trajectories of \hat{S}_1 (red solid line) and \hat{S}_2 (black dashed line) in the time interval from 0 to 10 ns, where switching takes place.

the SyAF dynamics, in Figs. 4(c) and (g) we plotted the amplitude of overall SyAF magnetization, defined as $m = |\hat{S}_1 + \hat{S}_2|$. This parameter vanishes for antiparallel alignment of both spins of CFL, but becomes nonzero when the configuration deviates from the antiparallel one. Magnetization of SyAF is also a measure of the CFL coupling to external magnetic field. Furthermore, Figs. 4(d) and (h) show the corresponding time variation of the resistance, R , which might be directly extracted from experimental measurements as well. In addition, in Figs. 4(e) and (i) we show the trajectories of \hat{S}_1 and \hat{S}_2 in the real space taken from the time interval from $t = 0$ to 10 ns. In addition, from Figs. 4(a) it has been found that the point where the threshold current reaches its maxi-

mum is located at $H_0 \simeq H_z^{02}$, which indicates its relation to magnetostatic interaction of F2 and fixed polarizer. This also has been confirmed by analogical simulations disregarding the magnetostatic coupling between magnetic layers, which resulted in similar diagram, but with $H_0 = 0$ (not shown). This fact significantly facilitates understanding the mechanism of SyAF switching.

The initial configuration assumed above was $-\hat{S}_1 = \hat{S}_2 \simeq \hat{S}_0$ with $\hat{S}_0 = \hat{e}_z$ ($\downarrow\uparrow$). When the magnitude of current density is large enough and $I < 0$, orientation of \hat{S}_1 becomes unstable and \hat{S}_1 starts to precess with small angle around $-\hat{e}_z$. Initial precession of \hat{S}_1 induces precession of \hat{S}_2 – mainly via the RKKY coupling. Generally, response to the exchange field is slower than current-induced dynamics. Therefore, a difference in precession phase of \hat{S}_2 and \hat{S}_1 appears, and configuration of SyAF deviates from the initial antiparallel one. This in turn enhances the STT acting on F2, which tends to switch \hat{S}_2 . Its amplitude, however, is small in comparison to the strong RKKY coupling. Further scenario of the dynamics depends then on the external magnetic field. When $H_{\text{app}} < H_0$ [Figs. 4(b – e)] the Zeeman energy of \hat{S}_2 has a maximum in the initial state and external magnetic field tends to switch \hat{S}_2 to the opposite orientation. Competition between the torques acting on SyAF results in out-of-plane precessions of both spins. After several precessions \hat{S}_1 reaches the opposite static state, which is stable due to STT. In turn, \hat{S}_2 is only slightly affected by STT, and its dynamics is damped in the external magnetic and RKKY exchange fields. In contrast, when $H_{\text{app}} > H_0$ [Figs. 4(f – i)], Zeeman energy of F2 has a local minimum in the initial state, which stabilizes \hat{S}_2 . Therefore, in a certain range of current density, SyAF does not switch but remains in self-sustained coherent in-plane precessions (red area in the upper part of Fig. 4(a)). For a sufficient current density, the SyAF structure becomes destabilized and the precessional angle increases until the spins pass the (x, y) -plane. Consequently, the precessional angle decreases and spins of the SyAF are stabilized in the opposite state ($\uparrow\downarrow$). Moreover, as shown in Fig. 4(c), the switching process for $H_{\text{app}} < H_0$ is connected with high distortion of SyAF configuration, where m in a certain point reaches its maximum value (corresponding to parallel orientation of both spins). Contrary, the m remains small for $H_{\text{app}} > H_0$ [Figs. 4(g)], and the effective magnetic moment of the free layer stays smaller than magnetic moment of a single layer. This might play an important role in applications of spin-torque devices based on CFLs.

The two switching mechanisms described above dominate the current-induced dynamics when the current density is close to the dynamics threshold. For higher current densities, the nonlinearities in SyAF dynamics become more pronounced, which results in bistable behavior of the dynamics, especially for $H_{\text{app}} < H_0$ and $I \gtrsim 10^8 \text{ Acm}^{-2}$. In that region, the number of out-of-plane precessions before SyAF switching increases with the current density. However, their precessional angle

increases in time and consequently \hat{S}_1 might reach an out-of-plane static point slightly tilted away from the \hat{e}_x direction while $\hat{S}_2 = \hat{e}_z$ remains in the layers plane. The out-of-plane static states (marked as $\leftarrow\uparrow$) have small resistance and appear as dark red spots in the diagram shown in Fig. 4(a).

In addition, from the analysis of the dispersion of pillar resistance (not shown) one finds that except of a narrow region close to the dynamics threshold with persistent in-plane precessions, no significant steady-state dynamics of SyAF element appears. As will be shown below, such a behavior might be observed when CFL becomes asymmetric (SyF free layer).

C. Synthetic ferrimagnet

Let us study now spin valve with SyF as a free layer, assuming $d_1 = 4$ nm and $d_2 = 2$ nm. Accordingly, $H_{\text{RKKY}2}$ remains 2 kOe while $H_{\text{RKKY}1}$ is reduced to 1 kOe. As in the case of SyAF, from the averaged time-dependent part of the pillar resistance we have constructed a diagram presenting current-induced dynamics, see Fig. 5(a). The static part of resistance is now $R_{\text{sp}} = 19.80$ Ωm^2 . The diagram has some features similar to those studied in the previous subsection. However, the maximum critical current is shifted towards negative values of H_{app} , even if magnetostatic interaction between magnetic layers is neglected. This asymmetry is caused by the difference in exchange and demagnetization fields acting on layers F_1 and F_2 . Moreover, this difference leads to more complex dynamics of the CFL's spins than that in the case of SyAF.

Generally, there are several dynamic regimes to be distinguished. The first one is the region of switching from $\uparrow\downarrow$ configuration to the opposite one, $\downarrow\uparrow$, which is located at largest values of H_{app} in the diagram. Mechanism of the switching is similar to that of SyAF shown in Figs. 4(f–i), where CFL changes its configuration just *via* in-plane precessional states with a small value of m (weak distortion of the antiparallel alignment of \hat{S}_1 and \hat{S}_2). Furthermore, the darker area above H_0 indicates one of the possible self-sustained dynamic regimes of SyF, i.e. the in-plane precessions (IPP); see Figs. 5(b–e). This precessional regime starts directly after the SyF switching, and \hat{S}_1 and \hat{S}_2 precess around \hat{e}_z and $-\hat{e}_z$, respectively. Due to different effective fields in F_1 and F_2 , and energy gains due to STT, the spins precess with different precessional angles [Fig. 5(e)] and consequently different frequencies. Because of the strong interlayer coupling and spin transfer between the layers, amplitudes of their precessions are periodically modulated in time. This modulation appears also in the time dependence of pillar resistance. Conversely, below H_0 the dynamic is dominated by large angle out-of-plane precessions (OPP) of both spins, as shown in Figs. 5(f–i). This dynamic state is connected with a strong distortion of the antiparallel CFL configuration, i.e. large value of m , and large variation of the

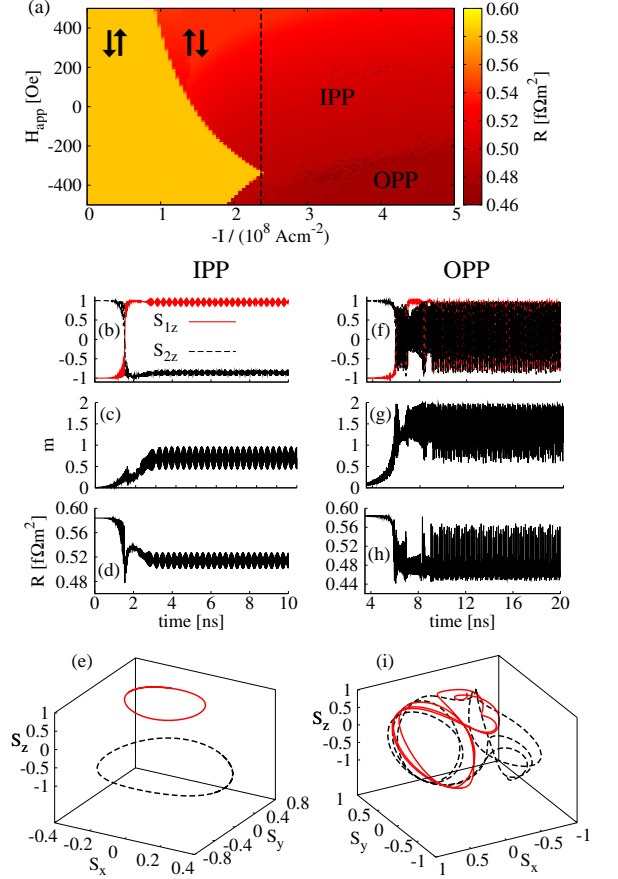


FIG. 5. (color online) (a) Averaged resistance of Cu-IrMn(10)/Py(8)/Cu(8)/Co(4)/Cu(1)/Co(2)-Cu spin valve pillar with a SyF free layer, presented as a function of current density and applied magnetic field. Examples of current-induced dynamics for $I = -3 \times 10^8$ Am^{-1} and $H_{\text{app}} = 200$ Oe (b–e) and $H_{\text{app}} = -400$ Oe (f–i). Panels (b) and (f) show dynamics of z -components of \hat{S}_1 and \hat{S}_2 , (c) and (g) present the overall magnetization of the free layer, (d) and (h) show the corresponding variation of pillar resistance, (e) and (i) show spin trajectories of \hat{S}_1 (red solid line) and \hat{S}_2 (black dashed line) taken from a time interval as large as 30 ns after 100 ns of initial equilibration.

resistance. From Fig. 5(i) one can see that trajectories of \hat{S}_1 and \hat{S}_2 are rather complicated including both IPP and OPP regimes with dominant OPP.

D. Power spectral density

From the analysis of current-induced dynamics we found that self-sustained dynamics in structures with SyF free layer is much richer than that in systems with SyAF free layer [see Figs. 5(b–i)]. Therefore, in this section we restrict ourselves to dynamic regimes of the SyF free layer only. More specifically, we shall examine the power spectral density (PSD) as a function of current density and external magnetic field.

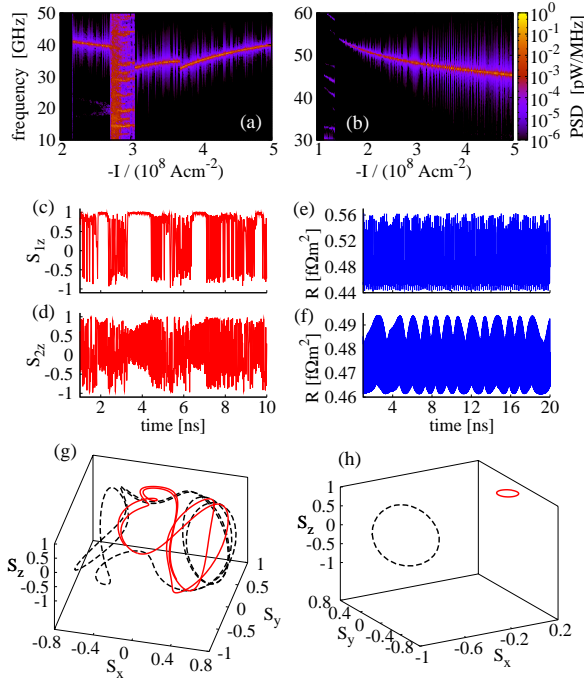


FIG. 6. Power spectral density calculated for the spin valve with SyF free layer at $T_{\text{eff}} = 5$ K and $H_{\text{app}} = -400$ Oe (a) and 200 Oe (b). (c) and (d) show steady time evolution of spins z -components in a time window of 10 ns after the equilibration at $H_{\text{app}} = -400$ Oe and $I = -2.8 \times 10^8 \text{ Acm}^{-2}$. (e) and (f) show steady time evolution of the time-dependent part of spin valve resistance in a time window of 20 ns after the equilibration at $H_{\text{app}} = -400$ Oe and $I = -3.6 \times 10^8 \text{ Acm}^{-2}$ (both \hat{S}_1 and \hat{S}_2 precess out of layer plane) and $I = -3.8 \times 10^8 \text{ Acm}^{-2}$ (\hat{S}_2 performs out-of-plane precessions while \hat{S}_1 precesses in the layer's plane), respectively. Panels (g) and (h) depict trajectories of \hat{S}_1 (red solid line) and \hat{S}_2 (black dashed line) corresponding to resistance oscillations (e) and (f), respectively.

In the simulation we started from $I = 0$ and changed current density in steps $\Delta I = 10^6 \text{ Acm}^{-2}$ at a fixed applied field. As before, to protect the SyF dynamics from collapsing into collinear static state, we assumed small thermal fluctuations corresponding to $T_{\text{eff}} = 5$ K. At each step we simulated the dynamics of coupled CFL's spins and calculated PSD. As in Ref. 29, we assumed that the input current is split between a load with resistance R_L and pillar with resistance $R_{\text{sp}} + R(t)$. Hence, voltage on the pillar has been calculated as $U(t) = IR(t)/[1 + R_{\text{sp}}/(R_L S)]$, where we assumed $R_L = 50 \Omega$, and S is the cross-section of the pillar (ellipsoid with the major and minor axes equal to 130 and 60 nm, respectively). Then, at a given I we calculated voltage in the frequency domain, $U(f)$, using fast Fourier transformation over the period $t_{\text{FFT}} = 50$ ns following the equilibration time of $t_{\text{eq}} = 30$ ns. The power spectral density has been defined as $\text{PSD}(f) = 2U^2(f)/(R_L \Delta f)$, where $\Delta f = 1/t_{\text{FFT}}$.

Figures 6(a) and (b) show PSD calculated at $H_{\text{app}} =$

-400 Oe and 200 Oe, respectively. The former case corresponds to that part of the diagram in Fig. 5(a), which includes OPP modes, while in the latter case we observed IPP only. Let us analyze first the situation in Fig. 6(a). When current passes through the corresponding threshold value, both spins start precessing in the layers' plane, similarly as shown in Fig. 5(b). Apart from the main peak in the PSD at $f \simeq 40$ GHz, two additional minor peaks close to $f \simeq 20$ GHz are visible. We attribute them to the oscillations of precessional amplitudes of both spins. With increasing amplitude of the current density, the precessional angles of both spins increase and their precessional frequencies slightly decrease. Moreover, with increasing current the frequencies of the minor peaks become closer and closer, until they finally coincide. At this point the PSD becomes widely distributed along the whole range of observed frequencies, which is an evidence of noisy variation of the resistance. An example of spin dynamics in this region is shown in Figs. 6(c) and (d) which have been taken in a time window as large as 10 ns after the equilibration period for $H_{\text{app}} = -400$ Oe and $I = -2.8 \times 10^8 \text{ Acm}^{-2}$ [within the broad feature of PSD in Fig. 6(a)]. Firstly, the figures show that \hat{S}_2 starts to perform out-of-plane precessions as a result of the competition between STT and RKKY coupling. Secondly, one can note thermally activated random transitions of \hat{S}_1 between OPP and IPP modes. These random transitions modify OPP precessions of \hat{S}_2 as well. Simultaneous dynamics of both spins causes chaotic variation of spin valve resistance and broadens the PSD. The quasi-chaotic feature of the spin dynamics in this range of current densities can be seen also on the spin trajectories, which cover almost the whole sphere (not shown).

Further increase in current density leads to stabilization of the OPP mode of \hat{S}_1 . Hence spin valve resistance becomes more periodic [see Fig. 6(e)] and PSD reveals a narrow peak again. Since both spins perform rather complicated dynamics including IPP but dominated by OPP regime [see Fig. 6(g)], we observe a blue-shift in PSD with current, which is connected with a decrease in the precessional angles. However, at a certain value of I we notice an abrupt drop in the peak's frequency. At this current density the STT acting on the left interface of layer F_1 starts to dominate the dynamics of \hat{S}_1 and enables only small angle IPPs along the \hat{S}_0 direction, which modifies the trajectory of \hat{S}_2 . \hat{S}_2 still remains in the OPP regime [see Fig. 6(h)] and hence the blue-shift with current appears. The fact that IPP of \hat{S}_1 still influence the dynamics of the whole SyF is also shown in Fig. 6(f), which presents the dynamic part of the spin valve resistance at $I = -3.8 \times 10^8 \text{ Acm}^{-2}$ and $H_{\text{app}} = -400$ Oe. As a result of IPPs of \hat{S}_1 , amplitude of the resistance varies periodically. In addition, comparison of Figs. 6(e) and (f) shows that the simultaneous OPPs of both spins lead to stronger variation of the resistance than in the case when the layers are in the IPP state.

Contrary, at $H_{\text{app}} = 200$ Oe one observes only IPP modes of both spins similar to those shown in Fig. 5(e).

The in-plane precessional angle increases with current density and hence the peak frequency in PSD decreases and becomes broader. In real systems, however, one might expect the peaks narrower than those obtained in the macrospin simulations, as observed in standard spin valves with a simple free layer^{30,31}.

IV. CRITICAL CURRENTS

First, we derive some approximate expressions for critical current density needed to induce dynamics of CFL, derived from linearized LLG equation. In metallic structures, the out-of-plane torque components are generally much smaller than the in-plane ones, and therefore will be omitted in the analytical considerations of this section ($b_1^{(0)}, b_1^{(2)}, b_2^{(1)} \rightarrow 0$).

The coupled LLG equations in spherical coordinates can be then written as

$$\frac{d\tilde{\mathbf{S}}}{dt} = \frac{1}{1 + \alpha^2} \bar{\mathbf{M}} \cdot \tilde{\mathbf{v}}, \quad (6)$$

where $\tilde{\mathbf{S}} = (\theta_1, \phi_1, \theta_2, \phi_2)^T$ is a 4-dimensional column vector which describes spin orientation in both layers constituting the CFL, and $\tilde{\mathbf{v}} = (v_{1\theta}, v_{1\phi}, v_{2\theta}, v_{2\phi})^T$ stands for the torque components, $v_{i\theta} = \mathbf{\Gamma}_i \cdot \hat{\mathbf{e}}_{i\theta}$ and $v_{i\phi} = \mathbf{\Gamma}_i \cdot \hat{\mathbf{e}}_{i\phi}$, with $\hat{\mathbf{e}}_{i\phi} = (\hat{\mathbf{e}}_z \times \hat{\mathbf{S}}_i) / \sin \theta_i$ and $\hat{\mathbf{e}}_{i\theta} = (\hat{\mathbf{S}}_i \times \hat{\mathbf{e}}_{i\phi}) / \sin \theta_i$ denoting unit vectors in local spherical coordinates associated with $\hat{\mathbf{S}}_i$. In turn, the 4×4 matrix $\bar{\mathbf{M}}$ takes the form

$$\bar{\mathbf{M}} = \begin{pmatrix} 1 & \alpha & 0 & 0 \\ -\alpha/\sin \theta_1 & 1/\sin \theta_1 & 0 & 0 \\ 0 & 0 & 1 & \alpha \\ 0 & 0 & -\alpha/\sin \theta_2 & 1/\sin \theta_2 \end{pmatrix}. \quad (7)$$

Static points of the CFL dynamics have to satisfy $v_{i\theta} = 0$ and $v_{i\phi} = 0$ for both $i = 1$ and $i = 2$. These conditions are obeyed in all collinear configurations, i.e. $\theta_i = 0, \pi$. Additional four trivial static points can be found in the out-of-plane configurations with $\theta_i = \pi/2$ and $\phi_i = 0, \pi$.

Following Ref. 23 we linearize Eq. (6) by expanding $\tilde{\mathbf{v}}$ into a series around the static points, which leads to

$$\frac{d\tilde{\mathbf{S}}}{dt} = \frac{1}{1 + \alpha^2} \bar{\mathbf{M}} \cdot \bar{\mathbf{J}} \cdot \tilde{\boldsymbol{\delta v}}, \quad (8)$$

where $\bar{\mathbf{J}}$ is a Jacobian matrix of $\partial \tilde{v}_i / \partial \tilde{S}_j$ components. The matrix product $\bar{\mathbf{M}} \cdot \bar{\mathbf{J}}$ defines here the dynamic matrix $\bar{\mathbf{D}} = \bar{\mathbf{M}} \cdot \bar{\mathbf{J}}$. This matrix allows one to study stability of CFL's spins in their static points. If $\text{Tr} \{\bar{\mathbf{D}}\}$ is negative, the static point is stable, otherwise it is unstable. Hence, the condition for critical current is³² $\text{Tr} \{\bar{\mathbf{D}}\} = 0$.

To obtain threshold current for dynamics onset of individual spins in the CFL, we assume first that one of the spins is fixed in its initial position and investigate stability of the second spin. The dynamic matrix $\bar{\mathbf{D}}$ becomes then reduced to a 2×2 matrix. Considering initial

position of SAF with $\hat{\mathbf{S}}_1 = -\hat{\mathbf{S}}_2 = -\hat{\mathbf{e}}_z$ (i.e. $\theta_1 = \pi$ and $\theta_2 = 0$), marked as $\uparrow\downarrow$, and polarizer $\hat{\mathbf{S}}_0 = \hat{\mathbf{e}}_z$, the stability condition leads to the following critical currents $I_{c1}^{\uparrow\downarrow}$ and $I_{c2}^{\uparrow\downarrow}$ for $\hat{\mathbf{S}}_1$ and $\hat{\mathbf{S}}_2$, respectively:

$$I_{c1}^{\uparrow\downarrow} = -\alpha \frac{\mu_0 M_s d_1}{a_1^{(0)} + a_1^{(2)}} \left[-H_{\text{ext}}^{\uparrow\downarrow} + H_{\text{ani}} - H_{\text{RKKY}1} + H_1^d \right], \quad (9)$$

with $H_{\text{ext}}^{\uparrow\downarrow} = H_{\text{app}} - H_z^{01} - H_z^{21}$, and

$$I_{c2}^{\uparrow\downarrow} = -\alpha \frac{\mu_0 M_s d_2}{a_2^{(1)}} \left[H_{\text{ext}}^{2\uparrow\downarrow} + H_{\text{ani}} - H_{\text{RKKY}2} + H_2^d \right], \quad (10)$$

with $H_{\text{ext}}^{2\uparrow\downarrow} = H_{\text{app}} - H_z^{02} - H_z^{12}$. In both above expressions $a_1^{(0)}$, $a_1^{(2)}$, and $a_2^{(1)}$ are taken in the considered static point, while the demagnetization field for the i -th layer is given by

$$H_i^d = \frac{H_{ix}^d + H_{iy}^d}{2} - H_{iz}^d. \quad (11)$$

Analogically, one can derive similar formulas for critical currents in the opposite ($\downarrow\uparrow$) magnetic configuration of the CFL.

Now we relax the assumption that one of the spins is fixed, and consider both spins of the CFL as free. Then, we calculate the trace of the whole 4×4 matrix, which leads to the following expression for critical current destabilizing the whole CFL:

$$I_{c\text{CFL}}^{\uparrow\downarrow} = -\alpha \frac{\mu_0 M_s d_1 d_2}{d_2(a_1^{(0)} + a_1^{(2)}) + d_1 a_2^{(1)}} \left[H_{\text{ext}}^{\uparrow\downarrow} + 2H_{\text{ani}} - H_{\text{RKKY}1} - H_{\text{RKKY}2} + H_1^d + H_2^d \right], \quad (12)$$

where $H_{\text{ext}}^{\uparrow\downarrow} = H_z^{01} - H_z^{02} + H_z^{21} + H_z^{12}$. Since the spins of CFL are antiparallel in the considered static point, $I_{c\text{CFL}}^{\uparrow\downarrow}$ is independent of external magnetic field. The above equation describes the critical current at which the CFL is destabilized as a rigid structure (unaffected by external magnetic field along the z -axis).

Numerical calculations presented below show that critical current is usually smaller than that given by Eq.(12). Apparently, as shown by numerical simulations, there is a phase shift in initial precessions of $\hat{\mathbf{S}}_1$ and $\hat{\mathbf{S}}_2$. Such a phase shift slightly perturbs initial antiparallel configuration and might reduce the critical current for the dynamics onset.

Similar formula also holds for the opposite configuration ($\downarrow\uparrow$), where the critical current is given by

$$I_{c\text{CFL}}^{\downarrow\uparrow} = \alpha \frac{\mu_0 M_s d_1 d_2}{d_2(a_1^{(0)} - a_1^{(2)}) - d_1 a_2^{(1)}} \left[-H_{\text{ext}}^{\downarrow\uparrow} + 2H_{\text{ani}} - H_{\text{RKKY}1} - H_{\text{RKKY}2} + H_1^d + H_2^d \right], \quad (13)$$

with $H_{\text{ext}}^{\uparrow\downarrow} = H_z^{01} - H_z^{02} - H_z^{21} - H_z^{12}$.

Now we discuss the theoretical results on critical currents in the context of those following from numerical simulations. Let us consider first the critical currents for individual spins of the SyAF free layer, assuming that the second spin remains stable in its initial position, Eqs. (9) and (10). The corresponding results obtained from the formula derived above are presented in Table I, where we have omitted a weak dependence on H_{app} . For the studied structure with SyAF free layer, $I_{c1}^{\uparrow\downarrow}$ is negative while $I_{c2}^{\uparrow\downarrow}$ is positive. From our analysis follows, that the current density at which dynamics appears in the simulations (Fig. 4(a)) is higher than that given by $I_{c1}^{\uparrow\downarrow}$. However, we checked numerically that the critical value $I_{c1}^{\uparrow\downarrow}$ agrees with the critical current obtained from simulations when assuming \hat{S}_1 as free and fixing \hat{S}_2 along \hat{e}_z .

	SyAF		SyF	
	$\uparrow\downarrow$	$\uparrow\downarrow$	$\uparrow\downarrow$	$\uparrow\downarrow$
I_{c1}	-0.31	0.43	-0.54	0.63
I_{c2}	0.98	-0.46	2.33	-0.78
I_{cCFL}	-0.86	0.87	-2.37	-9.18

TABLE I. Critical current densities in the units of 10^8 Acm^{-2} , calculated according to equations (9), (10), and (12) for both SyAF and SyF free layers.

Following the above discussion of the CFL dynamics, one can understand the shift of the threshold current as follows. Initially, when the current density exceeds $I_{c1}^{\uparrow\downarrow}$, \hat{S}_1 becomes destabilized. Then, \hat{S}_2 responds to the initial dynamics of \hat{S}_1 with similar coherent precession. However, \hat{S}_2 should still be stable in its initial position at this current density and common precessions of the two coupled spin moments damps the initial dynamics. Accordingly, SyAF ends up in the closest static state ($\uparrow\uparrow$). However, as the current density increases, the initial precessions of \hat{S}_1 become more pronounced, which in turn means that the initial antiparallel configuration becomes distorted and \hat{S}_2 becomes destabilized. This results in coupled dynamics of both spins and finally leads to switching of the SyAF structure.

On the other hand, we have also calculated the critical current for the whole SyAF structure according to Eq. (12), and for the given structure we got $I_{cCFL}^{\uparrow\downarrow}$ shown in Fig. 4(a) by the dashed vertical line (see also Table I). Equation (12) describes stability of the whole CFL, and since the interlayer coupling is strong, $I_{cCFL}^{\uparrow\downarrow}$ corresponds to the current density at which both spins become destabilized simultaneously preserving their antiparallel orientation. As can be seen in Fig. 4(a), this is the maximum threshold current density for current-induced dynamics. Because the rigid structure consisting of two antiparallel spins is not influenced by an external homogeneous magnetic field, there is no dependence of $I_{cCFL}^{\uparrow\downarrow}$

on H_{app} . Nevertheless, from our numerical simulation follows that the threshold current for the SyAF dynamics, I_{thr} , obeys the condition $|I_{c1}^{\uparrow\downarrow}| < |I_{\text{thr}}| < |I_{cCFL}^{\uparrow\downarrow}|$, provided that $|I_{c1}^{\uparrow\downarrow}| < |I_{c2}^{\uparrow\downarrow}|$ or (as in our case) $I_{c2}^{\uparrow\downarrow}$ has different sign.

When the SyAF is in the $\uparrow\downarrow$ configuration, the spin accumulation and spin current are different from those in the $\uparrow\uparrow$ configuration (at the same voltage). This in turn leads to different spin torques, which is the reason why the critical currents destabilizing $\uparrow\downarrow$ state are different from those for $\uparrow\uparrow$, as shown in Table I. From the critical currents one can expect relatively symmetric hysteresis with applied current in structures with SyAF. In contrast, $I_{cCFL}^{\uparrow\downarrow}$ for the SyF is negative, similarly as $I_{cCFL}^{\uparrow\downarrow}$, but it is significantly larger, which indicates lack of hysteresis. To compare switching of the SyAF and SyF free layers from the $\uparrow\uparrow$ to $\uparrow\downarrow$ configurations with the opposite one ($\uparrow\downarrow$ to $\uparrow\uparrow$), we have simulated dynamics of the corresponding CFLs assuming $H_{\text{app}} = 0$ and varying current density. The simulations have been performed in the quasistatic regime, i.e., for each value of current density the spin dynamics was first equilibrated for 50 ns and then averaged values of spin components and pillar resistance were calculated from the data taken for the next 30 ns of dynamics. In order to prevent the system from collapsing into a static state with zero torque, we have included a thermal stochastic field corresponding to $T_{\text{eff}} = 5 \text{ K}$ [see Eq. (3)]. Starting from $I = 0$ and going first towards negative currents we have constructed the current dependence of the averaged resistance and related z -components of both spins, as shown in Fig. 7. For both SyAF [Figs. 7(a–c)] and SyF [Figs. 7(d–f)] free layers, one can see relatively symmetric hysteresis with the current density. In both cases direct switching from $\uparrow\uparrow$ to $\uparrow\downarrow$ state occurs at a current density comparable to $I_{cCFL}^{\uparrow\downarrow}$. In contrast, in the case of SyF free layer, the second transition ($\uparrow\downarrow$ to $\uparrow\uparrow$) appears at a current density which is very different from that predicted by the linearized LLG model. Moreover, in both cases switching from $\uparrow\downarrow$ to $\uparrow\uparrow$ state does not appear directly, but through some precessional states. More precisely, as the positive current density increases, both spins start precessing in the layers' plane prior to switching. The in-plane precessions are connected with a significant drop in the resistance and with a reduction of the s_z -components. The range of IPP regime is particularly large in the case of SyF. From the analysis of spins' trajectories one may conclude that the angle of IPPs increases with increasing current density, and after exceeding a certain threshold angle CFL switches to the $\uparrow\uparrow$ configuration.

The other factor giving rise to the the difference in switching from $\uparrow\downarrow$ to $\uparrow\uparrow$ and from $\uparrow\uparrow$ to $\uparrow\downarrow$ follows from the fact that the magnetostatic interaction of the CFL's layers with the polarizer is different in the $\uparrow\uparrow$ and $\uparrow\downarrow$ states. To prove this we have constructed analogical hysteresis loops for SyAF and SyF free layers disregarding magnetostatic interaction with the F_0 layer; see Figs. 7(g) and

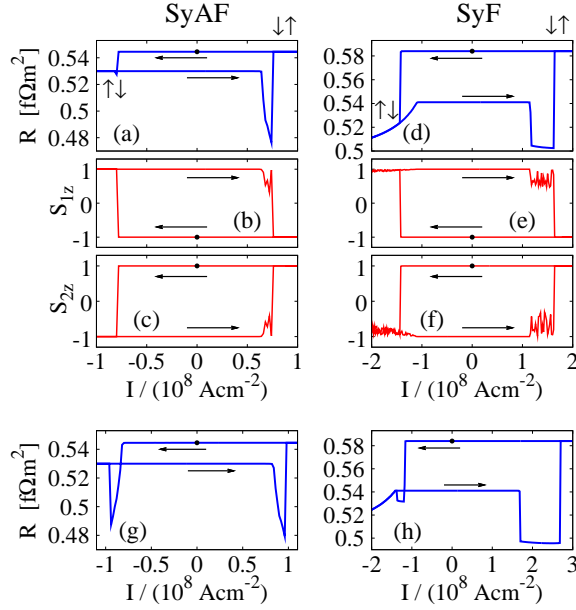


FIG. 7. Hysteresis loops of the resistance for the studied pillars with SyAF (a) and SyF (d) free layers. Panel (b) and (c) depict spin dynamics of \hat{S}_1 and \hat{S}_2 in SyAF, respectively, corresponding to resistance loop (a). Panels (e) and (f) show dynamics of \hat{S}_1 and \hat{S}_2 in SyF, respectively, corresponding to resistance loop (d). The initial point of each hysteresis loop is marked with a dot. The arrows indicate direction of the current change. Figures (g) and (h) correspond to the upper parts of (a) and (d), in which however the effects due to magnetostatic field of the reference layer to the CFL spins have been omitted.

(h). For both SyAF and SyF free layers we observe now large decrease in R for both switchings. This implies that both switchings are realized *via* in-plane precessions, in contrast to the case when F_0 influences the CFL dynamics via the corresponding magnetostatic field. While the hysteresis loop for SyAF remains symmetric, the one for SyF becomes highly asymmetric. The asymmetry of SyF loop is due to a significant asymmetry of STT in $\uparrow\downarrow$ and $\downarrow\uparrow$ states, which was previously shaded by the magnetostatic coupling with the layer F_0 .

V. DISCUSSION AND CONCLUSIONS

We have studied current-induced dynamics of SyAF and SyF composite free layers. By means of numerical simulations we identified variety of dynamical regimes. The most significant difference between dynamics of SyAF and SyF free layers concerns the evidence of self-sustained dynamics of both CFL spins. While in the case of SyAF only coupled in-plane precessions in a narrow window of external parameters (H_{app} and I) are observed, SyF free layer reveals more complex and richer dynamics, with the possibility of coupled out-of-plane precessions which might be interesting from the applica-

tion point of view. Furthermore, as shown by numerical simulations, both SyAF and SyF are switchable back and forth without the need of external magnetic field. For SyAF element two possible ways of switching have been identified. Since they lead to different switching times, their identification might be crucial for optimization of switching in real devices with SyAF free layers. However, one has to note that the diagrams shown in Figs. 4 and 5 may be changed when magnetization in CFL becomes non-homogeneous.

A disadvantage of the studied structures is their relatively low efficiency of switching, i.e. high amplitude of critical current and long switching time. In order to show more sophisticated ways of tuning the CFL devices, we have analyzed critical currents derived from the linearized LLG equation. The formula (12) has been identified as the maximum value of critical current at which dynamics of the CFL structure should be observed. This formula reveals some basic dependence of critical current on spin valve parameters, and therefore might be useful as an initial tool for its tuning. However, in some cases non-linear effects in CFL dynamics might completely change the process of CFL switching, as shown by the presented numerical simulations. But the effects of non-linear dynamics go beyond the simple approach of linearized LLG equation, and their study requires more sophisticated nontrivial methods and/or numerical simulations.

ACKNOWLEDGEMENTS

This work was supported by Polish Ministry of Science and Higher Education as a research project in years 2010-2011, and partly by EU through the Marie Curie Training Network SPINSWITCH (MRTN-CT-2006-035327). The authors thank M. Gmitra for helpful discussions. One of us (PB) also thanks L. López Díaz, E. Jaromirska, U. Ebels, and D. Gusakova for valuable suggestions.

Appendix A: Transformations of spin current

Torque acting on the left interface of F_1 is calculated from x and y components of $\mathbf{j}'_1 = \bar{\mathbf{T}}(\theta_1, \phi_1) \cdot \mathbf{j}_1$, where \mathbf{j}_1 is spin current vector in N_1 layer (written in global frame; shown in Fig. 1), and $\bar{\mathbf{T}}(\theta_1, \phi_1) = \bar{\mathbf{R}}_x(-\theta_1) \bar{\mathbf{R}}_z(\phi_1 - \pi/2)$, where $\bar{\mathbf{R}}_q(\alpha)$ is the matrix of rotation by angle α along the axis q in the counterclockwise direction when looking towards origin of the coordinate system. Hence \mathbf{j}'_1 components can be written as

$$j'_{1x} = j_{1x} \sin \phi_1 - j_{1y} \cos \phi_1, \quad (\text{A1a})$$

$$j'_{1y} = (j_{1x} \cos \phi_1 + j_{1y} \sin \phi_1) \cos \theta_1 - j_{1z} \sin \theta_1, \quad (\text{A1b})$$

$$j'_{1z} = (j_{1x} \cos \phi_1 + j_{1y} \sin \phi_1) \sin \theta_1 + j_{1z} \cos \theta_1, \quad (\text{A1c})$$

where (θ_1, ϕ_1) are spherical coordinates of \hat{S}_1 in the global frame. Similarly, we define torques' amplitudes

on the left interface of F_2 from the components of transformed spin current vector $\mathbf{j}_2''' = \bar{\mathbf{T}}(\theta_2, \phi_2) \cdot \mathbf{j}_2$. In this case, however, \mathbf{j}_2 is not written in the global frame, but in the local coordination system coordinate system connected with $\hat{\mathbf{S}}_1$. To rotate local coordinate system of $\hat{\mathbf{S}}_1$ to local coordinate system of $\hat{\mathbf{S}}_2$ we need to know spherical angles θ_2 and ϕ_2 of vector $\hat{\mathbf{S}}_2$ in the local coordinate system of $\hat{\mathbf{S}}_1$. This might be done by transforming first $\hat{\mathbf{S}}_2$ vector to local coordinate system of $\hat{\mathbf{S}}_1$ as $\hat{\mathbf{S}}_2' = \bar{\mathbf{T}}(\theta_1, \phi_1) \cdot \hat{\mathbf{S}}_2$ and calculate its angles θ_2 and ϕ_2 . Then we can calculate components of \mathbf{j}_2''' similarly as for

the left interface

$$j_{2x}''' = j_{2x} \sin \phi_2 - j_{2y} \cos \phi_2, \quad (\text{A2a})$$

$$j_{2y}''' = (j_{2x} \cos \phi_2 + j_{2y} \sin \phi_2) \cos \theta_2 - j_{2z} \sin \theta_2, \quad (\text{A2b})$$

$$j_{2z}''' = (j_{2x} \cos \phi_2 + j_{2y} \sin \phi_2) \sin \theta_2 + j_{2z} \cos \theta_2, \quad (\text{A2c})$$

Equation in N_2 , which is adjacent non-magnetic interface from the right-hand side of F_1 , are written in local coordinate system of $\hat{\mathbf{S}}_1$. To apply the definition of a_{12} and b_{12} we need to rotate the local coordinate system so, that its y -axis will lie in the layer given by vectors $\hat{\mathbf{S}}_1$ and $\hat{\mathbf{S}}_2$. This might be done by single rotation of local coordinate system around its z -axis by angle $\phi_2 - \pi/2$, $\mathbf{j}_2'' = \bar{\mathbf{R}}_z(\phi_2 - \pi/2) \cdot \mathbf{j}_2$, where

$$j_{2x}'' = j_{2x} \sin \phi_2 - j_{2y} \cos \phi_2, \quad (\text{A3a})$$

$$j_{2y}'' = j_{2x} \cos \phi_2 + j_{2y} \sin \phi_2, \quad (\text{A3b})$$

$$j_{2z}'' = j_{2z}. \quad (\text{A3c})$$

Note, angle ϕ_2 is calculated for vector $\hat{\mathbf{S}}_2$ transformed into coordinate system of $\hat{\mathbf{S}}_1$ as in previous case.

-
- ¹ J. C. Slonczewski, J. Magn. Magn. Mater. **159**, L1 (1996).
² L. Berger, Phys. Rev. B **54**, 9353 (1996).
³ M. Tsoi, A. G. M. Jansen, J. Bass, W.-C. Chiang, M. Seck, V. Tsoi, and P. Wyder, Phys. Rev. Lett. **80**, 4281 (1998).
⁴ J. A. Katine, F. J. Albert, R. A. Buhrman, E. B. Myers, and D. C. Ralph, Phys. Rev. Lett. **84**, 3149 (2000).
⁵ S. Serrano-Guisan, K. Rott, G. Reiss, J. Langer, B. Ocker, and H. W. Schumacher, Phys. Rev. Lett. **101**, 087201 (2008).
⁶ D. E. Nikonov, G. I. Bourianoff, G. Rowlands, and I. N. Krivorotov, J. Appl. Phys. **107**, 113910 (2010).
⁷ L. Liu, T. Moriyama, D. C. Ralph, and R. A. Buhrman, Appl. Phys. Lett. **94**, 122508 (2009).
⁸ P. Baláz, M. Gmitra, and J. Barnaś, Phys. Rev. B **79**, 144301 (2009).
⁹ S. S. P. Parkin and D. Mauri, Phys. Rev. B **44**, 7131 (1991).
¹⁰ P. Grünberg, R. Schreiber, Y. Pang, M. B. Brodsky, and H. Sowers, Phys. Rev. Lett. **57**, 2442 (1986).
¹¹ J.-V. Kim, T. Devolder, C. Chappert, C. Maufroid, and R. Fournel, Appl. Phys. Lett. **85**, 4094 (2004).
¹² T. Ochiai, Y. Jiang, A. Hirohata, N. Tezuka, S. Sugimoto, and K. Inomata, Appl. Phys. Lett. **86**, 242506 (2005).
¹³ N. Smith, S. Maat, M. J. Carey, and J. R. Childress, Phys. Rev. Lett. **101**, 247205 (2008).
¹⁴ S.-W. Lee and K.-J. Lee, Journal of Magnetism **15**, 149 (2010).
¹⁵ C.-T. Yen, W.-C. Chen, D.-Y. Wang, Y.-J. Lee, C.-T. Shen, S.-Y. Yang, C.-H. Tsai, C.-C. Hung, K.-H. Shen, M.-J. Tsai, et al., Appl. Phys. Lett. **93**, 092504 (2008).
¹⁶ C.-Y. You, J. Appl. Phys. **107**, 073911 (2010).
¹⁷ S. Mao, A. Mack, E. Singleton, J. Chen, S. S. Xue, H. Wang, Z. Gao, J. Li, and E. Murdock, J. Appl. Phys. **87**, 5720 (2000).
¹⁸ S. Urazhdin, Phys. Rev. B **78**, 060405(R) (2008).
¹⁹ D. Gusakova, D. Houssameddine, U. Ebels, B. Dieny, L. Buda-Prejbeanu, M. C. Cyrille, and B. Delaët, Phys. Rev. B **79**, 104406 (2009).
²⁰ D. Houssameddine, J. F. Sierra, D. Gusakova, B. Delaët, U. Ebels, L. D. Buda-Prejbeanu, M.-C. Cyrille, B. Dieny, B. Ocker, J. Langer, et al., Appl. Phys. Lett. **96**, 072511 (2010).
²¹ J. Barnaś, A. Fert, M. Gmitra, I. Weymann, and V. K. Dugaev, Phys. Rev. B **72**, 024426 (2005).
²² M. Gmitra and J. Barnaś, in *Toward Functional Nanomaterials*, edited by Z. Wang (Springer, 2009), pp. 285 – 322.
²³ Y. B. Bazaliy, B. A. Jones, and S.-C. Zhang, Phys. Rev. B **69**, 094421 (2004).
²⁴ U. Ebels, D. Houssameddine, I. Firastrau, D. Gusakova, C. Thirion, B. Dieny, and L. D. Buda-Prejbeanu, Phys. Rev. B **78**, 024436 (2008).
²⁵ A. J. Newell, W. Williams, and D. J. Dunlop, J. Geophys. Res. **98**, 9551 (1993).
²⁶ M. D. Stiles and A. Zangwill, Phys. Rev. B **66**, 014407 (2002).
²⁷ M. Gmitra and J. Barnaś, Phys. Rev. B **79**, 012403 (2009).
²⁸ M. Gmitra and J. Barnaś, Phys. Rev. Lett. **96**, 207205 (2006).
²⁹ S. Urazhdin, W. L. Lim, and A. Higgins, Phys. Rev. B **80**, 144411 (2009).
³⁰ J. C. Sankey, I. N. Krivorotov, S. I. Kiselev, P. M. Braganca, N. C. Emley, R. A. Buhrman, and D. C. Ralph, Phys. Rev. B **72**, 224427 (2005).
³¹ J.-V. Kim, Phys. Rev. B **73**, 174412 (2006).
³² S. Wiggins, *Introduction to Applied Nonlinear dynamical Systems and Chaos* (Springer-Verlag, 1990).